

Astrolabe: Steering Forward-Process Reinforcement Learning for Distilled Autoregressive Video Models

Songchun Zhang¹, Zeyue Xue^{2,3}, Siming Fu², Jie Huang², Xianghao Kong¹, Yue-Ma¹, Haoyang Huang², Nan Duan^{2§}, and Anyi Rao^{1§}

¹HKUST ²JD Explore Academy ³HKU

[Project Page](#)

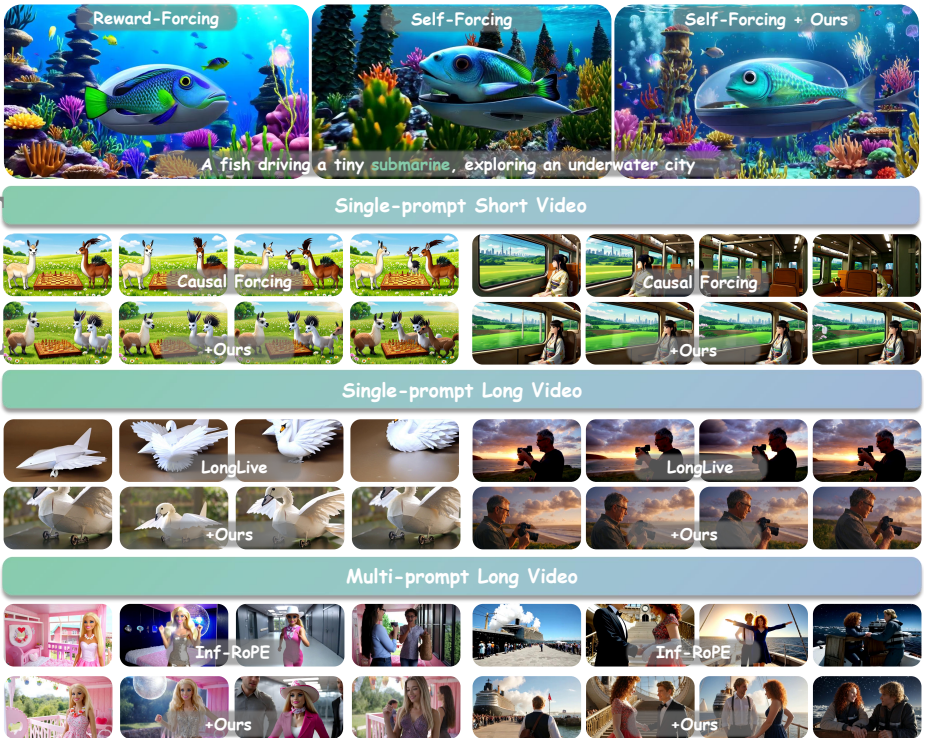


Fig. 1: *Astrolabe* efficiently aligns distilled streaming video models with human preferences without re-distillation, enhancing baselines (e.g., Causal Forcing [64], LongLive [51] and Infinite-RoPE [53]) by mitigating artifacts and improving temporal consistency. We demonstrate boosted perceptual quality across: (Top) single-prompt short, (Middle) single-prompt long, and (Bottom) multi-prompt long video generation.

Abstract. Distilled autoregressive (AR) video models enable efficient streaming generation but frequently misalign with human visual preferences. Existing reinforcement learning (RL) frameworks are not naturally suited to these architectures, typically requiring either expensive

arXiv:2603.17051v1 [cs.CV] 17 Mar 2026

re-distillation or solver-coupled reverse-process optimization that introduces considerable memory and computational overhead. We present Astrolabe, an efficient online RL framework tailored for distilled AR models. To overcome existing bottlenecks, we introduce a forward-process RL formulation based on negative-aware fine-tuning. By contrasting positive and negative samples directly at inference endpoints, this approach establishes an implicit policy improvement direction without requiring reverse-process unrolling. To scale this alignment to long videos, we propose a streaming training scheme that generates sequences progressively via a rolling KV-cache, applying RL updates exclusively to local clip windows while conditioning on prior context to ensure long-range coherence. Finally, to mitigate reward hacking, we integrate a multi-reward objective stabilized by uncertainty-aware selective regularization and dynamic reference updates. Extensive experiments demonstrate that our method consistently enhances generation quality across multiple distilled AR video models, serving as a robust and scalable alignment solution.

Keywords: Video Generation · Distilled Autoregressive Models · Reinforcement Fine-tuning

1 Introduction

Recent advances in diffusion models [4, 5, 8, 14, 17, 18, 42, 48, 59, 61, 63] have enabled unprecedented quality in video synthesis, yet deploying these systems for real-time interactive applications remains challenging. Conventional video diffusion models rely on extensive multi-step denoising processes, resulting in prohibitive generation latencies. Furthermore, the bidirectional attention mechanism employed by most architectures processes all frames jointly, precluding streaming generation, wherein frames must be produced sequentially. These constraints have motivated a paradigm shift toward efficient, autoregressive alternatives.

To overcome these constraints, several distilled autoregressive models [9, 20, 22, 23, 37, 51] have emerged. These methods distill pretrained bidirectional video diffusion models into efficient autoregressive models via distribution matching distillation (DMD) [54]. The resulting models leverage KV-caching for streaming inference, enabling real-time generation with the potential to support long video generation. However, while distillation ensures the student mimics the teacher’s distribution, it lacks optimization for human preference. Consequently, the generated outputs frequently exhibit artifacts and unnatural motion dynamics, remaining misaligned with human preferences.

Concurrently, online RL has demonstrated high efficacy in aligning LLMs with human preferences [12, 33]. This success motivates a natural question: *can online RL be applied to align distilled streaming video models with human visual expectations without reverting to computationally expensive pre-training or re-distillation pipelines?* Aligning these models via existing methods introduces non-trivial challenges. Previous attempts at reward-guided distillation [30] merely bias the supervised distillation loss by prioritizing samples with higher rewards. While this shifts the output distribution toward high-reward regions,

it lacks a mechanism for active exploration and fails to penalize suboptimal generation samples. On the other hand, applying online RL via reverse-process optimization [28, 49] requires log-probability estimation along the sampling trajectory. This couples the algorithm to specific solvers and necessitates storing intermediate trajectory states, adding substantial memory and computational overhead that erodes the efficiency advantages of streaming models.

We present **Astrolabe**, an efficient and stable online RL framework for distilled AR video models, as shown in Figure 2. Firstly, to bypass the limitations of reward-weighted distillation and the overhead of reverse-process RL, we introduce a trajectory-free alignment strategy tailored for distilled AR video generation. Drawing on the principles of negative-aware fine-tuning [62], our approach contrasts positive and negative generations to establish an implicit policy improvement direction. Requiring only clean inference endpoints, our method sidesteps solver-specific unrolling and full trajectory storage, better preserving the efficiency inherent to streaming architectures. Then, while this resolves per-clip alignment efficiently, scaling to long videos remains challenging; naively unrolling and backpropagating through extended sequences is prohibitively expensive. To address this, we introduce a streaming training scheme that generates videos progressively while applying RL updates only to short segments, conditioning on prior context to retain long-range coherence. Furthermore, to prevent models from reward hacking at the expense of overall aesthetics, the framework employs a multi-reward formulation covering visual quality, motion dynamics, and text alignment. This optimization process is further stabilized by an uncertainty-aware selective regularization strategy that restricts KL penalties to samples lacking auxiliary consensus, alongside a dynamic reference update mechanism that accommodates shifting distributions during online learning.

Extensive experiments on various distilled AR models validate the effectiveness of our method. Figure 1 showcases a diverse set of representative results, demonstrating that the proposed framework consistently enhances generation quality across different settings. Comprehensive evaluations demonstrate improvements across multiple benchmarks. In summary, the primary contributions of our work are as follows: (1) Astrolabe, an online reinforcement learning framework formulated to align distilled streaming video models with human visual preferences; (2) a streaming training scheme that enables scalable alignment of long videos via segment-wise optimization under historical context; and (3) a suite of stabilization techniques, encompassing multi-reward optimization and dynamic regularization, to mitigate reward hacking.

2 Related Work

2.1 Video Generative Models

Diffusion models achieve remarkable success in video synthesis [4, 5, 8, 14, 17, 18, 38, 48, 57, 59, 61]. The strong scalability of Diffusion Transformers (DiTs) [2, 34] facilitates the emergence of large-scale models [3, 27, 42, 52] that generate high-quality content by jointly denoising all frames. However, this full-sequence gen-

eration requires simultaneous processing of all frames, which incurs substantial latency and precludes real-time interaction. Consequently, autoregressive approaches [10, 19, 26, 45–47, 50, 58, 60] emerge to enable streaming generation by producing frames sequentially.

2.2 Autoregressive Video Generation

To circumvent the limitation of bidirectional diffusion models, autoregressive (AR) approaches enable streaming generation by producing frames sequentially. While AR models are inherently suitable for real-time applications, early methods [11, 21] relying on Teacher Forcing (TF) suffer from severe error accumulation during long-video synthesis. Recent studies explore novel training paradigms to resolve this train-test misalignment. Diffusion Forcing [6] introduces conditioning at arbitrary noise levels, while CausVid [55] employs block causal attention and distills bidirectional teacher via DMD [54]. More recently, Self-Forcing [22] and its successors [9, 13, 30, 51, 53] establish post-training frameworks that systematically mitigate error accumulation. Identifying an architectural gap in the initial ODE distillation phase of these frameworks, Causal Forcing [64] reveals that distilling from a bidirectional teacher violates frame-level injectivity. By employing an AR teacher for initialization instead, it theoretically bridges this gap to achieve superior real-time generation.

2.3 Reinforcement Learning for Generative Models

Recent successes in large language models [12, 33] highlight the efficacy of on-policy reinforcement learning via memory-efficient algorithms like GRPO [36]. For diffusion models, DiffusionDPO [41] utilizes off-policy pairs, while Dance-GRPO [49] and Flow-GRPO [28] perform alignment by estimating reverse-trajectory log-probabilities. These reverse-process methods inherently couple the training objective to specific solvers and demand full trajectory storage. To bypass this, DiffusionNFT [62] introduces solver-agnostic forward-process policy optimization. Building on this, WorldCompass [44] recently adapted NFT to autoregressive world models [39]. However, their framework directly optimizes heavy pre-distilled teacher models. Extending RL to highly efficient distilled AR video models remains an open problem.

3 Methodology

Given a distilled autoregressive video diffusion model optimized for real-time generation, our goal is to further align it with human preferences through online reinforcement learning in the post-training stage. We propose Astrolabe, a memory-efficient framework combining streaming rollout with forward-process RL optimization. Section 3.1 reviews the foundations of AR video diffusion and forward-process RL. Section 3.2 details our memory-efficient streaming rollout

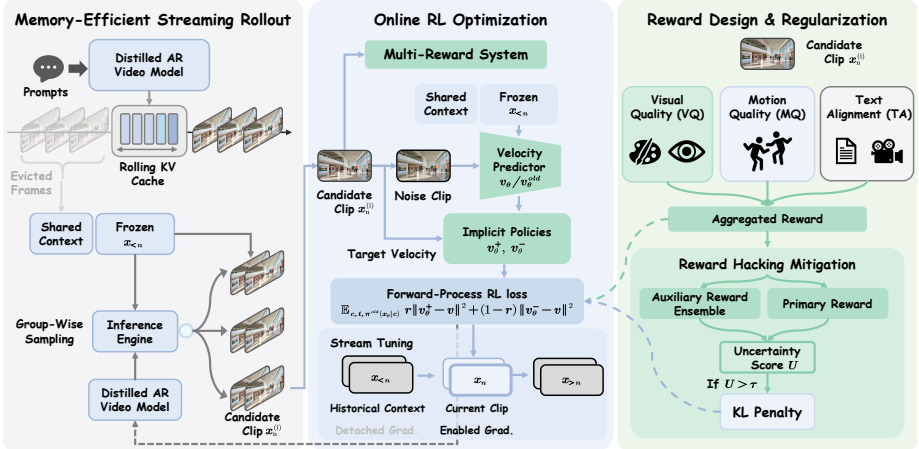


Fig. 2: Overview of Astrolabe. We propose a memory-efficient RL framework for distilled streaming video models. The method combines group-wise streaming rollout using a rolling KV cache for efficient group-wise sampling (see left), and clip-level forward-process RL for solver-agnostic optimization (see middle). To scale to long videos, we utilize Streaming Long Tuning with detached historical gradients. Furthermore, a multi-reward formulation paired with uncertainty-based selective regularization is employed to effectively mitigate reward hacking during training (see right). The pseudocode of the algorithm can be found in the supplementary materials.

mechanism for scalable exploration. Section 3.3 presents the online RL optimization strategy, encompassing clip-level forward-process RL and streaming long tuning. Finally, Section 3.4 formulates our multi-reward design and selective regularization approach to mitigate reward hacking.

3.1 Preliminaries

Autoregressive Video Diffusion Models. AR video model factorizes the joint distribution as $p(x_{1:N}) = \prod_{i=1}^N p(x_i | x_{<i})$. Following the flow matching formulation, each conditional $p(x_i | x_{<i})$ is modeled by defining a probability path $x_i^t = (1 - t)x_i + t\epsilon_i$, where $\epsilon_i \sim \mathcal{N}(0, I)$ and $t \in [0, 1]$. The model predicts the velocity field v_{θ} conditioned on text c and the KV cache of preceding frames. Training paradigms such as Teacher Forcing (TF) and Diffusion Forcing (DF) minimize the frame-wise MSE between the predicted and true targets. In TF, timesteps t are shared across frames with clean ground-truth context $x_{<i}$, whereas in DF, independent timesteps t_i are sampled for each frame using noisy context $x_{<i}^{t_j}$. Both suffer from exposure bias due to the mismatch between training context and inference-time generation. To mitigate this, Self-Forcing [22] employs autoregressive rollouts $\{x_{1:N}^{\theta}\} \sim \prod_{i=1}^N p_{\theta}(x_i | x_{<i})$ to simulate inference dynamics. The objective aligns the velocity predictions of the model on these self-generated trajectories with the scores provided by teacher model.

Forward-Process Reinforcement Learning. To avoid the likelihood estimation challenges of reverse-process RL, DiffusionNFT [62] optimizes diffusion models by applying rewards directly to the forward process. Given a clean generated sample x with a normalized reward $\tilde{r} \in [0, 1]$, a noisy version x^t is constructed for timestep $t \in [0, 1]$. Using the current (v_θ) and old ($v_{\theta_{\text{old}}}$) velocity predictors, implicit positive and negative policies are defined via interpolation:

$$v^+ = (1 - \beta)v_{\theta_{\text{old}}} + \beta v_\theta, \quad v^- = (1 + \beta)v_{\theta_{\text{old}}} - \beta v_\theta \quad (1)$$

where β controls the interpolation strength. The policy loss contrasts these implicit policies against the target forward velocity v_{target} :

$$\mathcal{L}_{\text{policy}} = \tilde{r} \|v^+ - v_{\text{target}}\|_2^2 + (1 - \tilde{r}) \|v^- - v_{\text{target}}\|_2^2 \quad (2)$$

This trajectory-free formulation requires only clean generated samples, enabling highly efficient, solver-agnostic training.

3.2 Memory-Efficient Streaming Rollout

Standard RL paradigms rely on sequence-level rollouts with global rewards. For autoregressive (AR) video generation, this introduces two critical bottlenecks: the temporal credit assignment problem, where sparse global scores fail to isolate localized visual degradation, and the prohibitive memory overhead of maintaining independent KV caches for long sequences. To overcome these limitations, we propose a group-wise streaming rollout strategy.

Rolling KV Cache with Frame Sinks. We maintain a rolling KV cache to bound memory usage. Let the sequence of generated clips be denoted as x_1, x_2, \dots, x_N . At generation step n , naïvely caching the full history $x_{<n}$ incurs a KV memory cost that grows linearly with video length, quickly becoming prohibitive for long-horizon rollouts. To resolve this, we construct a restricted visual context window \mathcal{C}_n comprising two components: a *frame sink* of S permanently retained frames that anchors global semantic context to prevent long-range drift, and a rolling window of the L most recent frames that provides fine-grained local conditioning. The model attends exclusively to the KV cache of \mathcal{C}_n to generate the next clip $x_n \sim \pi_\theta(\cdot | \mathcal{C}_n, c)$. Since S and L are fixed hyperparameters independent of total video length N , the resident KV memory remains constant regardless of how long the video grows, enabling real-time streaming rollout.

Clip-level Group-wise Sampling. Rather than generating G independent long trajectories from scratch, we autoregressively sample the visual history exactly once and freeze its KV cache as a shared prefix. At the n -th step, utilizing the memory-efficient KV states of \mathcal{C}_n , the model decodes G independent candidate clips in parallel:

$$x_n^{(i)} \sim \pi_\theta(\cdot | \mathcal{C}_n, c), \quad \text{for } i \in \{1, \dots, G\} \quad (3)$$

This clip-level rollout restricts the generation overhead to the local chunk rather than the full sequence. By sharing the frozen context prefix across all G candidates, the additional cost of group-wise sampling is incurred only once per

step rather than once per trajectory, substantially reducing rollout time and eliminating out-of-memory bottlenecks during reinforcement learning.

3.3 Online RL Optimization

Clip-level Forward-Process RL. For each candidate $x_n^{(i)}$, we evaluate a composite reward $R(x_n^{(i)}, c)$ and compute its advantage $A^{(i)}$ via group-wise mean-centering:

$$A^{(i)} = R(x_n^{(i)}, c) - \frac{1}{G} \sum_{j=1}^G R(x_n^{(j)}, c) \quad (4)$$

This advantage is then normalized as $\tilde{r}_i = \text{clip}(A^{(i)}/A_{\max})/2 + 0.5$. For our $T = 4$ distilled model, the timestep t is sampled from $\mathcal{T}_{\text{distill}}$. Crucially, we discard the adaptive loss weighting of DiffusionNFT [62], as it triggers gradient explosion under large discretization gaps in distilled AR settings. Conditioned on text c and the shared KV cache \mathcal{C}_n , we construct the noised sample $x_n^{t,(i)}$ to predict velocities v_θ and $v_{\theta_{\text{old}}}$. The model is optimized directly via the implicit policy loss $\mathcal{L}_{\text{policy}}$ (Eq. 2) by substituting $x_n^{t,(i)}$ to derive v_{target} . To further mitigate reward hacking, this objective is complemented by an uncertainty-aware selective KL penalty (Section 3.4).

Streaming Long Tuning. Distilled AR models suffer from a train-short/test-long mismatch, where accumulated prediction errors cause inevitable long-horizon degradation. To address this, our training paradigm strictly simulates the dynamics of long-sequence inference while decoupling the forward rollout from gradient computation. Specifically, we first perform a full forward pass to accumulate the KV cache up to the target step. Upon reaching the active training window x_n , the KV cache of all preceding frames $x_{<n}$ is explicitly detached from the computation graph. This detached cache serves as historical context, mimicking the progressively noisy conditions encountered during autoregressive generation. Gradients are then backpropagated through the active window. This exact formulation inherently bounds the training memory usage, circumventing the cost of backpropagation through extended trajectories.

3.4 Reward Design and Regularization

Multi-reward Formulation. Scalar reward functions obscure specific quality dimensions and often inadvertently encourage the model to exploit one attribute over others. To address this, we formulate a composite reward integrating three distinct axes: Visual Quality (VQ), Motion Quality (MQ), and Text-Video Alignment (TA). We compute the Visual Quality (VQ) reward as the mean HPSv3 [31] score over the top 30% of frames. Excluding lower-scoring frames prevents transient motion blur from disproportionately penalizing the overall aesthetic assessment. For the Motion Quality (MQ) reward, we evaluate temporal consistency using a pre-trained VideoAlign [29] strictly on grayscale inputs; removing color forces the metric to focus on motion dynamics rather than texture. Finally, the

Text Alignment (TA) reward employs the standard RGB VideoAlign to measure the semantic correspondence between the text and the generated video

Uncertainty-Aware Penalty. To prevent uniform KL regularization from indiscriminately suppressing high-quality generations, we introduce a selective KL penalty targeting reward hacking via reward rank disagreement [16]. For each candidate $x_n^{(i)}$, we quantify sample uncertainty as the rank discrepancy between the primary reward model p and $M - 1$ auxiliary models: $\Delta_{\text{rank}}^{(i)} = \text{rank}_p^{(i)} - \frac{1}{M-1} \sum_{m \neq p} \text{rank}_m^{(i)}$. High positive values indicate likely reward hacking lacking ensemble consensus. We mask these risky samples using $\mathcal{M}^{(i)} = \mathbb{1}[\Delta_{\text{rank}}^{(i)} > \tau]$, where τ is the $(1 - \rho)$ -th percentile of positive discrepancies (with risk ratio ρ). The total objective $\mathcal{L} = \mathcal{L}_{\text{policy}} + \lambda_{\text{KL}} \mathcal{L}_{\text{KL}}$ applies the KL penalty strictly to masked samples, preserving optimization flexibility for clean data. Furthermore, to mitigate distributional shifts during online RL, the policy θ_{old} follows an EMA update, and the reference policy conditionally resets ($\theta_{\text{ref}} \leftarrow \theta$) when policy deviation surpasses τ_{KL} or epochs reach K_{max} .

4 Experiments

4.1 Experimental Setup

Implementation Details. To validate the effectiveness of our method, we evaluate Astrolabe on distilled autoregressive models. We adopt base models trained via Self-Forcing [22], Causal-Forcing [64], and LongLive [51] as our primary baselines. Training prompts are sampled from the VidProM dataset [43], specifically utilizing the filtered subset introduced in DanceGRPO [49]. We employ Low-Rank Adaptation (LoRA) with rank $r = 256$ and scaling factor $\alpha = 256$ for parameter-efficient fine-tuning. To maximize memory efficiency during optimization, we do not store separate full-parameter copies for the current policy v_θ and the old policy $v_{\theta_{\text{old}}}$. Instead, both policies share a single frozen base model, and we switch between their respective lightweight LoRA during the forward pass, reducing GPU memory overhead. Training operations are distributed across 48 NVIDIA H200 GPUs. Each epoch processes 48 prompts, maintaining a group size of $G = 24$ candidate clips per prompt. For reward computation, we integrate VideoAlign [29] and HPSv3 [31] into our pipeline. More details can be found in supplementary material.

4.2 Short-Video Single-Prompt Generation

We first validate our method under the short-video, single-prompt setting. Following VBench protocols [24], we evaluate models using 946 standard prompts. To ensure a fair comparison with Self-Forcing, we utilize the augmented prompt test set during sampling, where prompts are expanded via Qwen2.5-7B-Instruct [1] using Wan2.1 [42] system prompts. We integrate Astrolabe with various distilled AR models, comparing them against native AR models and bidirectional diffusion baselines. Quantitative results in Table 1 show that Astrolabe consistently

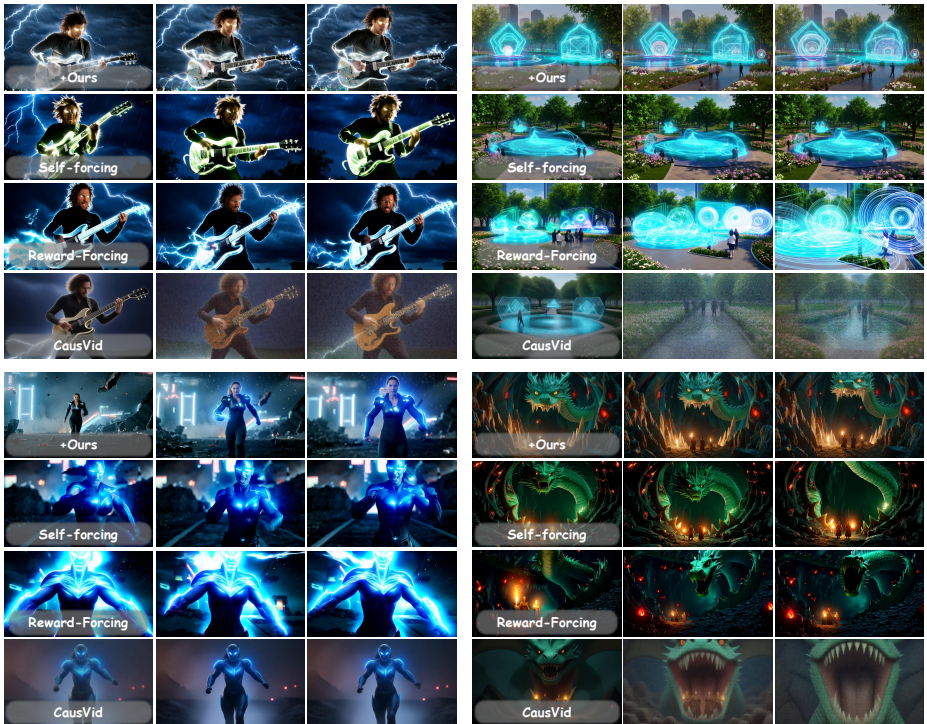


Fig. 3: Qualitative comparison under the short-video, single-prompt setting. We evaluate our framework (+Ours) against other baselines. Visual results confirm that our method generates videos with significantly sharper textures and superior motion coherence, aligning better with human preferences. More results can be found in supplementary material.

enhances performance across all Self-Forcing variants. Similar gains observed in LongLive [51] and Causal-Forcing [64] further demonstrate the framework’s generalizability across different base architectures. To further assess alignment with human preferences, we curate 100 diverse prompts from MovieGenBench [35] for evaluation. We compute HPSv3 and Motion Quality scores to quantify improvements in aesthetic appeal and temporal consistency. Results indicate that our RL-tuned models outperform their base versions in these metrics while maintaining the exact inference speed of the original checkpoints. Qualitative results in Figure 3 further confirm that Astrolabe yields sharper textures and superior motion coherence without sacrificing system throughput.

4.3 Long-Video Single-Prompt Generation

Under the single-prompt long-video generation setting, we evaluate our method using VBench-Long protocols. For each prompt in the official dataset, we generate a 30-second video and subsequently partition it into localized clips using

Table 1: Quantitative results on VBench benchmarks. Integrating our approach into existing distilled models yields consistent improvements in motion quality, semantic alignment, and overall generation quality.

Method	Total↑	Quality↑	Semantic↑	HPSv3↑	MQ↑	Throughput↑
Diffusion Models						
LTX-Video [15]	80.00	82.30	70.79	8.32	1.34	8.98
Wan2.1 [42]	84.26	85.30	80.09	9.26	1.62	0.78
AR Models						
SkyReels-V2 [7]	82.67	84.70	74.53	9.08	1.59	0.49
MAGI-1 [40]	79.18	82.04	67.74	7.95	1.52	0.19
NOVA [10]	80.12	80.39	79.05	8.21	1.63	0.88
PyramidFlow [25]	81.72	84.74	69.62	8.76	1.50	6.70
Distilled AR Models						
CausVid [55]	81.20	84.05	69.80	7.56	1.22	17.0
Reward Forcing [30]	84.13	84.84	81.32	8.74	1.65	23.1
Self-Forcing [22]	83.74	84.48	80.77	9.36	1.65	17.0
+ Ours	83.79 ⁺⁰⁵	84.51 ⁺⁰³	80.92 ⁺¹⁵	10.72 ^{+1.36}	1.71 ⁺⁰⁶	17.0
LongLive [51]	83.22	83.68	81.37	9.38	1.51	20.7
+ Ours	84.93 ^{+1.71}	85.83 ^{+2.15}	81.36 ^{-.01}	11.03 ^{+1.65}	1.64 ^{+1.13}	20.7
Causal Forcing [64]	84.04	84.59	81.84	9.48	1.69	17.0
+ Ours	84.46 ⁺⁴²	85.15 ⁺⁵⁶	81.72 ^{-.12}	10.84 ^{+1.36}	1.80 ^{+1.11}	17.0

Table 2: Quantitative results on VBench-Long benchmarks. Integrating our method consistently improves the performance of long video generation baselines across both video quality and human preference metrics.

Method	Total↑	Quality↑	Semantic↑	HPSv3↑	MQ↑
SkyReels-V2 [7]	75.29	80.77	53.37	8.72	1.54
FramePack [56]	81.95	83.61	75.32	8.94	1.58
Self-Forcing [22]	81.59	83.82	72.70	9.12	1.61
+ Ours	82.03	84.36	72.71	10.38	1.72
LongLive [51]	83.52	85.44	75.82	9.21	1.48
+ Ours	84.07	86.12	75.87	10.67	1.64
Causal Forcing [64]	82.87	84.36	76.91	9.28	1.65
+ Ours	84.24	86.18	76.48	10.52	1.74

the standard VBench-Long evaluation scripts. Notably, while LongLive natively supports long-video generation, Self-Forcing and Causal-Forcing are exclusively trained on 5-second sequences. To enable long-horizon generation for these short-context models, we integrate the Infinity-RoPE [53] to extrapolate their positional embeddings. Furthermore, we rigorously benchmark these configurations against open-source solutions, including SkyReels-V2 [7] and FramePack [56]. Quantitative results in Table 2 report standard VBench-Long metrics measuring long-horizon quality and temporal consistency. Results indicate that our RL framework can also improve performance across long-video benchmarks, demonstrating that alignment optimizations conducted on short videos can effectively extrapolate to extended temporal horizons. Qualitative results in Figure 4 further



Fig. 4: Qualitative results under the single-prompt long-video setting. Our framework (+Ours) effectively translates alignment optimizations from short videos to extended temporal horizons. Our approach delivers enhanced visual details and more stable throughout the sequence.

confirm that Astrolabe yields sharper textures and superior motion coherence over extended durations.

4.4 Long-Video Multi-Prompt Generation

To demonstrate that our framework effectively improves human preference alignment, we evaluate Astrolabe in the setting of interactive multi-prompt long-video generation. We apply our method directly to the baselines, demonstrating how Astrolabe further enhances their capabilities. Following established protocols from LongLive [51], we curate 100 groups of narrative scripts. Each group comprises six successive 10-second prompts, yielding 60-second long-form videos. To ensure fair comparisons, short-context baselines (Self-Forcing, Causal-Forcing) are adapted for multi-prompt generation via prompt switching during the autoregressive rollout. LongLive, conversely, natively supports generative extrapolation with interactive instructions. We segment the generated videos at prompt boundaries to evaluate text alignment. CLIP scores are subsequently computed at 10-second intervals to measure clip-wise semantic adherence. Quantitative results in Table 3 show that Astrolabe improves overall generation quality, with noticeable gains in visual aesthetics and long-range motion consistency. Qualitative examples in Figure 6 further illustrate these enhancements during extended

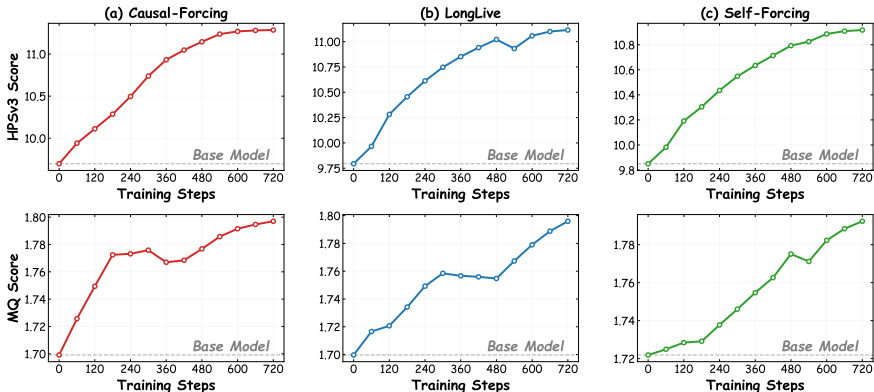


Fig. 5: Performance improvements across different models. We evaluate our method on three models. The dashed grey lines indicate the baseline performance of the respective base models. The results demonstrate that our approach consistently improves both HPSv3 and MQ scores across all three models.

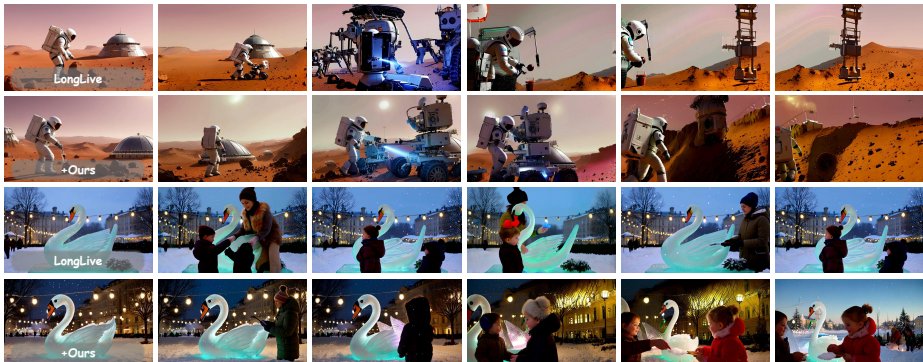


Fig. 6: Qualitative comparison of multi-prompt long-video generation. We compare the LongLive [51] with our method. The generated sequences exhibit noticeable improvements in visual aesthetics and fine details during complex narrative transitions.

video generation. These results suggest that our framework enhances both frame-level aesthetics and temporal consistency in complex multi-prompt setting.

4.5 Ablation Studies

We conduct ablation studies to validate each component of our method. All ablations are performed on Causal-Forcing with short-video alignment unless otherwise specified. Additional discussion and details can be found in the Supplementary Material.

Streaming Training Scheme. Table 4 compares different rollout and optimization strategies for 30-second video generation. Sequence-level rollout with full backpropagation causes out-of-memory errors. Our clip-level group-wise sampling with detached context achieves the best trade-off: it reduces memory con-

Table 3: Quantitative evaluation on long video generation. We compare these overall metrics alongside CLIP Scores evaluated across 10-second intervals (0-60s).

Method	Quality Score \uparrow	Consistency Score \uparrow	Aesthetic Score \uparrow	CLIP Score \uparrow					
				0-10	10-20	20-30	30-40	40-50	50-60
SkyReels-V2 [7]	81.55	94.72	56.83	25.31	23.40	22.50	21.62	21.67	20.91
FramePack [56]	84.40	96.77	59.44	26.51	22.60	22.18	21.53	21.98	21.62
Self-Forcing [22]	83.94	95.74	58.45	26.24	24.87	23.46	21.92	22.05	21.07
+ Ours	84.72	95.98	59.62	26.42	24.75	23.95	22.40	21.85	21.50
LongLive [51]	84.28	96.05	59.89	26.63	25.77	24.65	23.99	24.52	24.11
+ Ours	85.15	96.16	60.75	26.80	26.15	24.45	24.55	24.30	24.65
Causal-Forcing [64]	84.12	95.88	59.15	26.45	25.60	23.98	22.85	22.48	22.45
+ Ours	84.95	95.63	60.32	26.58	25.12	23.85	23.40	23.10	22.95

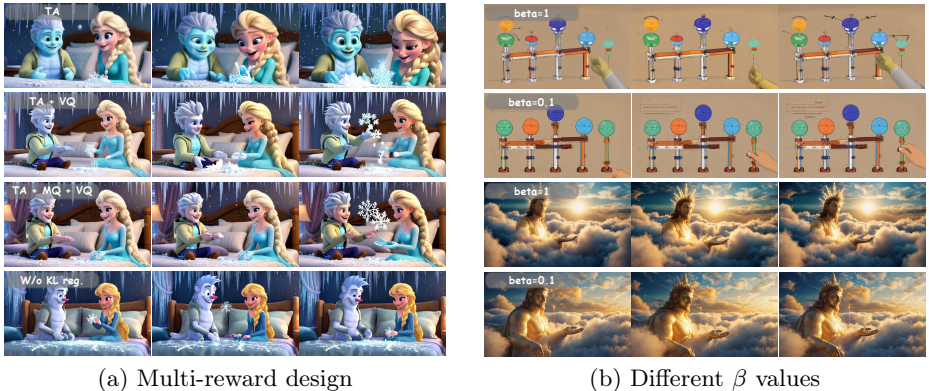


Fig. 7: Ablation studies on reward formulation and interpolation strength. (a) Optimizing a single objective induces reward hacking and degrades other quality dimensions, whereas our aggregated formulation balances visual aesthetics and motion consistency. (b) The parameter β controls the implicit contrast between positive and negative samples, with $\beta = 1.0$ yielding the optimal trade-off for quality.

sumption by $\approx 2\times$ compared to clip-level full backpropagation while improving both HPSv3 and MQ. The efficiency gains stem from sharing historical context across candidate clips reducing redundant computation.

Reward Design and Regularization. Table 4 ablates our objective formulation. Single-reward optimization induces hacking: VQ-only training collapses into static frames, improving HPSv3 but degrading MQ. Our multi-reward formulation (VQ+MQ+TA) prevents this single-objective overfitting, yielding balanced improvements. Furthermore, uniform KL regularization over-constrains learning, while its omission causes instability and early MQ plateaus (Figure 8a). Our selective KL penalty with EMA reference updates resolves this by adaptively penalizing only high-uncertainty predictions. This targeted approach preserves optimization freedom for confident samples, effectively balancing exploration with stable convergence across all metrics.

Removing Adaptive Weighting. DiffusionNFT [62] scales the loss using a self-normalized x_0 denominator. However, Figure 8b demonstrates this adaptive weighting destabilizes distilled AR setting. Under large discretization gaps, this dynamic denominator becomes volatile, causing the predicted x_0 norm to explode

Table 4: Ablation studies on each component. (a) and (b) show the impact of the streaming strategy and selective KL regularization. (c) compares different reward combinations.

(a) Streaming Training				(b) Selective KL Reg.			
Config	HPSv3 \uparrow	MQ \uparrow	Mem \downarrow	Strategy	HPSv3 \uparrow	MQ \uparrow	TA \uparrow
Seq + Full BP	OOM	OOM	>140	No KL	10.67	1.74	-0.068
Seq + Detach	10.21	1.72	96.4	Uni. ($\lambda = 1e^{-4}$)	10.52	1.71	0.012
Clip + Full BP	10.58	1.76	112.3	Uni. ($\lambda = 5e^{-4}$)	10.28	1.68	0.028
Clip+Detach	10.84	1.80	54.3	Sel.+EMA	10.84	1.80	0.065

(c) Multi-Reward Formulation									
Reward	HPSv3 \uparrow	MQ \uparrow	TA \uparrow	VB \uparrow	Reward	HPSv3 \uparrow	MQ \uparrow	TA \uparrow	VB \uparrow
Baseline	9.48	1.69	-0.015	84.04	VQ + MQ	10.67	1.74	-0.068	83.95
VQ only	10.92	1.58	-0.075	83.21	VQ + TA	10.71	1.62	0.055	84.12
MQ only	9.31	1.82	-0.058	83.67	MQ + TA	9.45	1.78	0.051	84.08
TA only	9.42	1.62	0.082	84.25	All (Ours)	10.84	1.80	0.065	84.46

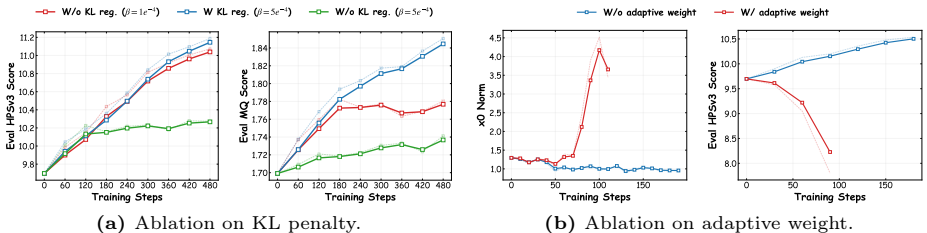


Fig. 8: Ablation study of stabilization techniques in Astrolabe. (a) Effect of the selective KL penalty. (b) Impact of the dynamic adaptive weight mechanism.

after 50 steps and triggering a sharp collapse in reward. Conversely, removing this scaling factor bounds the x_0 norm and ensures steady, monotonic reward improvements.

Impact of β . Figure 7 ablates the parameter β , which determines the scale of the implicit guidance direction integrated into the old policy. Empirical results indicate that varying β directly influences the temporal dynamics of the generated sequences. In our experimental setup, setting $\beta = 1$ yields higher overall visual and motion quality compared to a smaller value such as $\beta = 0.1$. Consequently, we adopt $\beta = 1$ as the default configuration to maintain generation stability.

5 Conclusion

We present Astrolabe, an online RL framework for aligning distilled autoregressive video models with human preferences. Utilizing a memory-efficient, forward-process RL formulation, our method eliminates the trajectory storage overhead of reverse-process alternatives. For long-video scalability, we introduce a streaming training scheme with local-window optimization, achieving constant peak memory. To prevent reward hacking, we implement a multi-reward formulation

coupled with an uncertainty-aware selective KL penalty. Extensive experiments across multiple distilled streaming architectures and benchmarks validate the effectiveness and generality of our approach.

References

1. Bai, J., Bai, S., Chu, Y., Cui, Z., Dang, K., Deng, X., Fan, Y., Ge, W., Han, Y., Huang, F., et al.: Qwen technical report. arXiv preprint arXiv:2309.16609 (2023) [8](#)
2. Bao, F., Nie, S., Xue, K., Cao, Y., Li, C., Su, H., Zhu, J.: All are worth words: A vit backbone for diffusion models. In: Proceedings of the IEEE/CVF conference on computer vision and pattern recognition. pp. 22669–22679 (2023) [3](#)
3. Bao, F., Xiang, C., Yue, G., He, G., Zhu, H., Zheng, K., Zhao, M., Liu, S., Wang, Y., Zhu, J.: Vidu: a highly consistent, dynamic and skilled text-to-video generator with diffusion models. arXiv preprint arXiv:2405.04233 (2024) [3](#)
4. Blattmann, A., Dockhorn, T., Kulal, S., Mendelevitch, D., Kilian, M., Lorenz, D., Levi, Y., English, Z., Voleti, V., Letts, A., et al.: Stable video diffusion: Scaling latent video diffusion models to large datasets. arXiv preprint arXiv:2311.15127 (2023) [2](#), [3](#)
5. Blattmann, A., Rombach, R., Ling, H., Dockhorn, T., Kim, S.W., Fidler, S., Kreis, K.: Align your latents: High-resolution video synthesis with latent diffusion models. In: Proceedings of the IEEE/CVF conference on computer vision and pattern recognition. pp. 22563–22575 (2023) [2](#), [3](#)
6. Chen, B., Martí Monsó, D., Du, Y., Simchowicz, M., Tedrake, R., Sitzmann, V.: Diffusion forcing: Next-token prediction meets full-sequence diffusion. *Advances in Neural Information Processing Systems* **37**, 24081–24125 (2024) [4](#)
7. Chen, G., Lin, D., Yang, J., Lin, C., Zhu, J., Fan, M., Zhang, H., Chen, S., Chen, Z., Ma, C., et al.: Skyreels-v2: Infinite-length film generative model. arXiv preprint arXiv:2504.13074 (2025) [10](#), [13](#)
8. Chen, H., Xia, M., He, Y., Zhang, Y., Cun, X., Yang, S., Xing, J., Liu, Y., Chen, Q., Wang, X., et al.: Videocrafter1: Open diffusion models for high-quality video generation. arXiv preprint arXiv:2310.19512 (2023) [2](#), [3](#)
9. Cui, J., Wu, J., Li, M., Yang, T., Li, X., Wang, R., Bai, A., Ban, Y., Hsieh, C.J.: Self-forcing++: Towards minute-scale high-quality video generation. arXiv preprint arXiv:2510.02283 (2025) [2](#), [4](#)
10. Deng, H., Pan, T., Diao, H., Luo, Z., Cui, Y., Lu, H., Shan, S., Qi, Y., Wang, X.: Autoregressive video generation without vector quantization. arXiv preprint arXiv:2412.14169 (2024) [4](#), [10](#)
11. Gao, K., Shi, J., Zhang, H., Wang, C., Xiao, J., Chen, L.: Ca2-vdm: Efficient autoregressive video diffusion model with causal generation and cache sharing. arXiv preprint arXiv:2411.16375 (2024) [4](#)
12. Guo, D., Yang, D., Zhang, H., Song, J., Zhang, R., Xu, R., Zhu, Q., Ma, S., Wang, P., Bi, X., et al.: Deepseek-r1: Incentivizing reasoning capability in llms via reinforcement learning. arXiv preprint arXiv:2501.12948 (2025) [2](#), [4](#)
13. Guo, Y., Yang, C., He, H., Zhao, Y., Wei, M., Yang, Z., Huang, W., Lin, D.: End-to-end training for autoregressive video diffusion via self-resampling. arXiv preprint arXiv:2512.15702 (2025) [4](#)
14. Gupta, A., Yu, L., Sohn, K., Gu, X., Hahn, M., Li, F.F., Essa, I., Jiang, L., Lezama, J.: Photorealistic video generation with diffusion models. In: European Conference on Computer Vision. pp. 393–411. Springer (2024) [2](#), [3](#)

15. HaCohen, Y., Chiprut, N., Brazowski, B., Shalem, D., Moshe, D., Richardson, E., Levin, E., Shiran, G., Zabari, N., Gordon, O., et al.: Ltx-video: Realtime video latent diffusion. arXiv preprint arXiv:2501.00103 (2024) **10**
16. He, H., Ye, Y., Liu, J., Liang, J., Wang, Z., Yuan, Z., Wang, X., Mao, H., Wan, P., Pan, L.: Gardo: Reinforcing diffusion models without reward hacking. arXiv preprint arXiv:2512.24138 (2025) **8**
17. He, Y., Yang, T., Zhang, Y., Shan, Y., Chen, Q.: Latent video diffusion models for high-fidelity long video generation. arXiv preprint arXiv:2211.13221 (2022) **2, 3**
18. Ho, J., Salimans, T., Gritsenko, A., Chan, W., Norouzi, M., Fleet, D.J.: Video diffusion models. *Advances in neural information processing systems* **35**, 8633–8646 (2022) **2, 3**
19. Hong, W., Ding, M., Zheng, W., Liu, X., Tang, J.: Cogvideo: Large-scale pretraining for text-to-video generation via transformers. arXiv preprint arXiv:2205.15868 (2022) **4**
20. Hong, Y., Mei, Y., Ge, C., Xu, Y., Zhou, Y., Bi, S., Hold-Geoffroy, Y., Roberts, M., Fisher, M., Shechtman, E., et al.: Relic: Interactive video world model with long-horizon memory. arXiv preprint arXiv:2512.04040 (2025) **2**
21. Hu, J., Hu, S., Song, Y., Huang, Y., Wang, M., Zhou, H., Liu, Z., Ma, W.Y., Sun, M.: Acddit: Interpolating autoregressive conditional modeling and diffusion transformer. arXiv preprint arXiv:2412.07720 (2024) **4**
22. Huang, X., Li, Z., He, G., Zhou, M., Shechtman, E.: Self forcing: Bridging the train-test gap in autoregressive video diffusion. arXiv preprint arXiv:2506.08009 (2025) **2, 4, 5, 8, 10, 13**
23. Huang, Y., Guo, H., Wu, F., Zhang, S., Huang, S., Gan, Q., Liu, L., Zhao, S., Chen, E., Liu, J., et al.: Live avatar: Streaming real-time audio-driven avatar generation with infinite length. arXiv preprint arXiv:2512.04677 (2025) **2**
24. Huang, Z., He, Y., Yu, J., Zhang, F., Si, C., Jiang, Y., Zhang, Y., Wu, T., Jin, Q., Chanpaisit, N., et al.: Vbench: Comprehensive benchmark suite for video generative models. In: *Proceedings of the IEEE/CVF Conference on Computer Vision and Pattern Recognition*. pp. 21807–21818 (2024) **8**
25. Jin, Y., Sun, Z., Li, N., Xu, K., Jiang, H., Zhuang, N., Huang, Q., Song, Y., Mu, Y., Lin, Z.: Pyramidal flow matching for efficient video generative modeling. arXiv preprint arXiv:2410.05954 (2024) **10**
26. Kondratyuk, D., Yu, L., Gu, X., Lezama, J., Huang, J., Schindler, G., Hornung, R., Birodkar, V., Yan, J., Chiu, M.C., et al.: Videopoet: A large language model for zero-shot video generation. arXiv preprint arXiv:2312.14125 (2023) **4**
27. Kong, W., Tian, Q., Zhang, Z., Min, R., Dai, Z., Zhou, J., Xiong, J., Li, X., Wu, B., Zhang, J., et al.: Hunyuanvideo: A systematic framework for large video generative models. arXiv preprint arXiv:2412.03603 (2024) **3**
28. Liu, J., Liu, G., Liang, J., Li, Y., Liu, J., Wang, X., Wan, P., Zhang, D., Ouyang, W.: Flow-grpo: Training flow matching models via online rl. arXiv preprint arXiv:2505.05470 (2025) **3, 4**
29. Liu, J., Liu, G., Liang, J., Yuan, Z., Liu, X., Zheng, M., Wu, X., Wang, Q., Xia, M., Wang, X., et al.: Improving video generation with human feedback. In: *The Thirty-ninth Annual Conference on Neural Information Processing Systems* (2025) **7, 8**
30. Lu, Y., Zeng, Y., Li, H., Ouyang, H., Wang, Q., Cheng, K.L., Zhu, J., Cao, H., Zhang, Z., Zhu, X., et al.: Reward forcing: Efficient streaming video generation with rewarded distribution matching distillation. arXiv preprint arXiv:2512.04678 (2025) **2, 4, 10**

31. Ma, Y., Wu, X., Sun, K., Li, H.: Hpsv3: Towards wide-spectrum human preference score. In: Proceedings of the IEEE/CVF International Conference on Computer Vision. pp. 15086–15095 (2025) **7, 8**
32. Millon, E.: Krea realtime 14b: Real-time video generation (2025), <https://github.com/krea-ai/realtime-video> **4**
33. Ouyang, L., Wu, J., Jiang, X., Almeida, D., Wainwright, C., Mishkin, P., Zhang, C., Agarwal, S., Slama, K., Ray, A., et al.: Training language models to follow instructions with human feedback. *Advances in neural information processing systems* **35**, 27730–27744 (2022) **2, 4**
34. Peebles, W., Xie, S.: Scalable diffusion models with transformers. In: Proceedings of the IEEE/CVF international conference on computer vision. pp. 4195–4205 (2023) **3**
35. Polyak, A., Zohar, A., Brown, A., Tjandra, A., Sinha, A., Lee, A., Vyas, A., Shi, B., Ma, C.Y., Chuang, C.Y., et al.: Movie gen: A cast of media foundation models. arXiv preprint arXiv:2410.13720 (2024) **9**
36. Shao, Z., Wang, P., Zhu, Q., Xu, R., Song, J., Bi, X., Zhang, H., Zhang, M., Li, Y., Wu, Y., et al.: Deepseekmath: Pushing the limits of mathematical reasoning in open language models. arXiv preprint arXiv:2402.03300 (2024) **4**
37. Shin, J., Li, Z., Zhang, R., Zhu, J.Y., Park, J., Shechtman, E., Huang, X.: Motion-stream: Real-time video generation with interactive motion controls. arXiv preprint arXiv:2511.01266 (2025) **2**
38. Singer, U., Polyak, A., Hayes, T., Yin, X., An, J., Zhang, S., Hu, Q., Yang, H., Ashual, O., Gafni, O., et al.: Make-a-video: Text-to-video generation without text-video data. arXiv preprint arXiv:2209.14792 (2022) **3**
39. Sun, W., Zhang, H., Wang, H., Wu, J., Wang, Z., Wang, Z., Wang, Y., Zhang, J., Wang, T., Guo, C.: Worldplay: Towards long-term geometric consistency for real-time interactive world modeling. arXiv preprint arXiv:2512.14614 (2025) **4**
40. Teng, H., Jia, H., Sun, L., Li, L., Li, M., Tang, M., Han, S., Zhang, T., Zhang, W., Luo, W., et al.: Magi-1: Autoregressive video generation at scale. arXiv preprint arXiv:2505.13211 (2025) **10**
41. Wallace, B., Dang, M., Rafailov, R., Zhou, L., Lou, A., Purushwalkam, S., Ermon, S., Xiong, C., Joty, S., Naik, N.: Diffusion model alignment using direct preference optimization. In: Proceedings of the IEEE/CVF Conference on Computer Vision and Pattern Recognition. pp. 8228–8238 (2024) **4**
42. Wan, T., Wang, A., Ai, B., Wen, B., Mao, C., Xie, C.W., Chen, D., Yu, F., Zhao, H., Yang, J., et al.: Wan: Open and advanced large-scale video generative models. arXiv preprint arXiv:2503.20314 (2025) **2, 3, 8, 10**
43. Wang, W., Yang, Y.: Vidprom: A million-scale real prompt-gallery dataset for text-to-video diffusion models. *Advances in Neural Information Processing Systems* **37**, 65618–65642 (2024) **8**
44. Wang, Z., Wang, T., Zhang, H., Zuo, X., Wu, J., Wang, H., Sun, W., Wang, Z., Cao, C., Zhao, H., et al.: Worldcompass: Reinforcement learning for long-horizon world models. arXiv preprint arXiv:2602.09022 (2026) **4**
45. Weissenborn, D., Täckström, O., Uszkoreit, J.: Scaling autoregressive video models. arXiv preprint arXiv:1906.02634 (2019) **4**
46. Wu, C., Huang, L., Zhang, Q., Li, B., Ji, L., Yang, F., Sapiro, G., Duan, N.: Godiva: Generating open-domain videos from natural descriptions. arXiv preprint arXiv:2104.14806 (2021) **4**
47. Wu, C., Liang, J., Ji, L., Yang, F., Fang, Y., Jiang, D., Duan, N.: Nüwa: Visual synthesis pre-training for neural visual world creation. In: European conference on computer vision. pp. 720–736. Springer (2022) **4**

48. Xing, J., Xia, M., Zhang, Y., Chen, H., Yu, W., Liu, H., Liu, G., Wang, X., Shan, Y., Wong, T.T.: Dynamicrafter: Animating open-domain images with video diffusion priors. In: European Conference on Computer Vision. pp. 399–417. Springer (2024) [2](#), [3](#)
49. Xue, Z., Wu, J., Gao, Y., Kong, F., Zhu, L., Chen, M., Liu, Z., Liu, W., Guo, Q., Huang, W., et al.: Dancegrpo: Unleashing grpo on visual generation. arXiv preprint arXiv:2505.07818 (2025) [3](#), [4](#), [8](#)
50. Yan, W., Zhang, Y., Abbeel, P., Srinivas, A.: Videogpt: Video generation using vq-vae and transformers. arXiv preprint arXiv:2104.10157 (2021) [4](#)
51. Yang, S., Huang, W., Chu, R., Xiao, Y., Zhao, Y., Wang, X., Li, M., Xie, E., Chen, Y., Lu, Y., et al.: Longlive: Real-time interactive long video generation. arXiv preprint arXiv:2509.22622 (2025) [1](#), [2](#), [4](#), [8](#), [9](#), [10](#), [11](#), [12](#), [13](#)
52. Yang, Z., Teng, J., Zheng, W., Ding, M., Huang, S., Xu, J., Yang, Y., Hong, W., Zhang, X., Feng, G., et al.: Cogvideox: Text-to-video diffusion models with an expert transformer. arXiv preprint arXiv:2408.06072 (2024) [3](#)
53. Yesiltepe, H., Meral, T.H.S., Akan, A.K., Oktay, K., Yanardag, P.: Infinity-rope: Action-controllable infinite video generation emerges from autoregressive self-rollback. arXiv preprint arXiv:2511.20649 (2025) [1](#), [4](#), [10](#)
54. Yin, T., Gharbi, M., Zhang, R., Shechtman, E., Durand, F., Freeman, W.T., Park, T.: One-step diffusion with distribution matching distillation. In: Proceedings of the IEEE/CVF conference on computer vision and pattern recognition. pp. 6613–6623 (2024) [2](#), [4](#)
55. Yin, T., Zhang, Q., Zhang, R., Freeman, W.T., Durand, F., Shechtman, E., Huang, X.: From slow bidirectional to fast autoregressive video diffusion models. In: Proceedings of the Computer Vision and Pattern Recognition Conference. pp. 22963–22974 (2025) [4](#), [10](#)
56. Zhang, L., Cai, S., Li, M., Wetzstein, G., Agrawala, M.: Frame context packing and drift prevention in next-frame-prediction video diffusion models. arXiv preprint arXiv:2504.12626 (2025) [10](#), [13](#)
57. Zhao, M., Bao, F., Li, C., Zhu, J.: Egsde: Unpaired image-to-image translation via energy-guided stochastic differential equations. *Advances in Neural Information Processing Systems* **35**, 3609–3623 (2022) [3](#)
58. Zhao, M., He, G., Chen, Y., Zhu, H., Li, C., Zhu, J.: Riflex: A free lunch for length extrapolation in video diffusion transformers. arXiv preprint arXiv:2502.15894 (2025) [4](#)
59. Zhao, M., Wang, R., Bao, F., Li, C., Zhu, J.: Controlvideo: conditional control for one-shot text-driven video editing and beyond. *Science China Information Sciences* **68**(3), 132107 (2025) [2](#), [3](#)
60. Zhao, M., Zhu, H., Wang, Y., Yan, B., Zhang, J., He, G., Yang, L., Li, C., Zhu, J.: Ultravico: Breaking extrapolation limits in video diffusion transformers. arXiv preprint arXiv:2511.20123 (2025) [4](#)
61. Zhao, M., Zhu, H., Xiang, C., Zheng, K., Li, C., Zhu, J.: Identifying and solving conditional image leakage in image-to-video diffusion model. *Advances in Neural Information Processing Systems* **37**, 30300–30326 (2024) [2](#), [3](#)
62. Zheng, K., Chen, H., Ye, H., Wang, H., Zhang, Q., Jiang, K., Su, H., Ermon, S., Zhu, J., Liu, M.Y.: Diffusionnft: Online diffusion reinforcement with forward process. arXiv preprint arXiv:2509.16117 (2025) [3](#), [4](#), [6](#), [7](#), [13](#), [1](#)
63. Zheng, Z., Peng, X., Yang, T., Shen, C., Li, S., Liu, H., Zhou, Y., Li, T., You, Y.: Open-sora: Democratizing efficient video production for all. arXiv preprint arXiv:2412.20404 (2024) [2](#)

64. Zhu, H., Zhao, M., He, G., Su, H., Li, C., Zhu, J.: Causal forcing: Autoregressive diffusion distillation done right for high-quality real-time interactive video generation. arXiv preprint arXiv:2602.02214 (2026) [1](#), [4](#), [8](#), [9](#), [10](#), [13](#)

A Hyperparameters

We provide detailed hyperparameter in Table S1.

Table S1: Comprehensive Hyperparameters for Astrolabe Training. We detail the configurations used across the model architecture, optimization, diffusion process, reinforcement learning, and streaming rollout.

Module	Hyperparameter	Value
Model & Video Specs	Base Architecture	Causal Wan 2.1
	Video Resolution ($H \times W$)	480 × 832
LoRA Fine-Tuning	Rank (r)	256
	Scaling Factor (α)	256
	Dropout Rate	0.0
	Gradient Checkpointing	True
Optimization	Hardware	48 × NVIDIA GPUs
	Precision Mode	bf16 (Mixed Precision)
	Optimizer	AdamW ($\beta_1 = 0.9, \beta_2 = 0.999$)
	Learning Rate (η)	1e-5
	Weight Decay	1e-4
	Epsilon (ϵ)	1e-8
Diffusion Process	Max Gradient Norm	1.0
	Distillation Timesteps (T)	4 (sampled from [1000, 750, 500, 250])
	Timestep Shift	5.0
	Forward Process Noise Level	0.7
Selective Regularization	Interpolation Strength (β)	1.0
	KL Penalty Weight (λ_{KL})	1e-4
	Advantage Clip Max	5.0
	Reward Normalization	Global Std with Per-Prompt Tracking
	EMA Decay Rate (γ)	0.9
Streaming Rollout	EMA Update Interval	1 step
	Window Selection Strategy	Random Choice
	Rolling Window Size (L)	21 (Self-Forcing) / 15 (Longlive)
	Frame Sink Size (S)	3

B Theoretical Proofs and Analysis

We extend the theoretical foundation of DiffusionNFT [62] from global, non-autoregressive continuous-time diffusion to the settings of autoregressive (AR) streaming generation and few-step distilled models. Specifically, we prove the optimality of local advantage guidance (Theorem 1), and establish a reward lower bound via selective KL penalty (Theorem 2).

B.1 Conditional Improvement via Advantage Guidance

Theorem 1 (Conditional Improvement via Advantage Guidance). *Let \mathcal{C}_n be the frozen context at step n , $\tilde{r}(x_n, \mathcal{C}_n) \in [0, 1]$ the normalized advantage, and $\alpha \triangleq \alpha(x_n^t, \mathcal{C}_n) = \mathbb{E}_{\pi_{\text{old}}}[\tilde{r} \mid x_n^t, \mathcal{C}_n]$ the posterior positive probability. Define the implicit positive/negative distributions:*

$$\pi^+(x_n \mid \mathcal{C}_n) = \frac{\tilde{r} \cdot \pi_{\text{old}}}{\mathbb{E}[\tilde{r}]}, \quad \pi^-(x_n \mid \mathcal{C}_n) = \frac{(1 - \tilde{r}) \cdot \pi_{\text{old}}}{\mathbb{E}[1 - \tilde{r}]} \quad (5)$$

and the local policy loss ($\beta > 0$ controls negative repulsion strength):

$$\mathcal{L}_{\text{policy}}^{(n)}(\theta) = \mathbb{E}_{t, x_n^t} \left[\|v_\theta - v^+\|^2 + \beta \|v_\theta - v^-\|^2 \right] \quad (6)$$

where v^\pm are conditional flow matching targets under π^\pm . Then the optimal velocity field satisfies:

$$v_\theta^* = v_{\text{old}} + \frac{1 - \alpha(1 + \beta)}{(1 + \beta)(1 - \alpha)} (v^+ - v_{\text{old}}) \quad (7)$$

which strictly shifts the local transition toward the advantage-weighted policy in the typical regime $\alpha(1 + \beta) < 1$.

Proof. Since the joint distribution factorizes as $p(x_{1:N}) = \prod_n p(x_n \mid \mathcal{C}_n)$, the velocity field at step n is strictly conditioned on \mathcal{C}_n . By Bayes' theorem, the posterior decomposes as:

$$\pi_{\text{old}}(x_n^0 \mid x_n^t, \mathcal{C}_n) = \alpha \pi^+(x_n^0 \mid x_n^t, \mathcal{C}_n) + (1 - \alpha) \pi^-(x_n^0 \mid x_n^t, \mathcal{C}_n) \quad (8)$$

By the law of total expectation, the baseline velocity inherits this mixture:

$$v_{\text{old}} = \alpha v^+ + (1 - \alpha) v^- \quad (9)$$

Let $\delta^+ = v^+ - v_{\text{old}}$. From Eq. (9), $v^- - v_{\text{old}} = -\frac{\alpha}{1 - \alpha} \delta^+$. Substituting into the loss and writing $u = v_\theta - v_{\text{old}}$:

$$\mathcal{L} = \mathbb{E} \left[\|u - \delta^+\|^2 + \beta \left\| u + \frac{\alpha}{1 - \alpha} \delta^+ \right\|^2 \right] \quad (10)$$

Setting $\partial \mathcal{L} / \partial u = 0$:

$$(1 + \beta) u^* = \delta^+ - \frac{\beta \alpha}{1 - \alpha} \delta^+ = \frac{1 - \alpha(1 + \beta)}{1 - \alpha} \delta^+ \quad (11)$$

which yields the stated result. When $\alpha > 0$ and $\alpha(1 + \beta) < 1$, the shift aligns with $v^+ - v_{\text{old}}$, pushing the model toward the high-advantage region. As $\beta \rightarrow 0$, this degrades to standard reward-weighted regression. Thus, optimizing the local advantage strictly improves $\pi_\theta(x_n \mid \mathcal{C}_n)$ without requiring gradients across the full trajectory.

B.2 Performance Lower Bound with Selective Trust Region

Theorem 2 (Performance Lower Bound with Selective Trust Region).

Let $\hat{R}(x)$ be the proxy reward, $R^*(x)$ the true preference with $|R^*| \leq R_{\max}$, and $\mathcal{U} = \{x \mid \Delta_{\text{rank}}(x) > \tau\}$ the high-uncertainty region. Assume:

- (A3) For $x \notin \mathcal{U}$: $|\hat{R}(x) - R^*(x)| \leq \epsilon_{\text{safe}}$.
- (A4) Under π_{ref} : $\mathbb{E}_{\pi_{\text{ref}}}[\|\hat{R} - R^*\mid x \in \mathcal{U}] \leq \epsilon_{\text{risk}}$, with $\epsilon_{\text{risk}} \gg \epsilon_{\text{safe}}$.

Define the selective velocity MSE in \mathcal{U} :

$$\mathcal{L}_{\text{KL}}(\theta) = \mathbb{E}_{x \sim \pi_\theta, x \in \mathcal{U}} \int_0^1 \frac{\|v_\theta(x_t, t) - v_{\text{ref}}(x_t, t)\|^2}{\sigma^2(t)} dt \quad (12)$$

Then the true reward of π_θ is lower-bounded by:

$$\mathbb{E}_{\pi_\theta}[R^*] \geq \mathbb{E}_{\pi_\theta}[\hat{R}] - \epsilon_{\text{safe}} - \pi_\theta(\mathcal{U})(\epsilon_{\text{risk}} + 2R_{\max}\sqrt{\mathcal{L}_{\text{KL}}}) \quad (13)$$

Proof. **Step 1: Regional decomposition.**

$$\mathbb{E}_{\pi_\theta}[R^*] = \mathbb{E}_{\pi_\theta}[R^* \mid x \notin \mathcal{U}] \cdot \pi_\theta(\mathcal{U}^C) + \mathbb{E}_{\pi_\theta}[R^* \mid x \in \mathcal{U}] \cdot \pi_\theta(\mathcal{U}) \quad (14)$$

Step 2: Safe region. By (A3), $\mathbb{E}_{\pi_\theta}[R^* \mid x \notin \mathcal{U}] \geq \mathbb{E}_{\pi_\theta}[\hat{R} \mid x \notin \mathcal{U}] - \epsilon_{\text{safe}}$.

Step 3: Risk region. Since (A4) holds for π_{ref} , transferring to π_θ requires bounding the distribution shift. By the TV dual representation with $|f| \leq 2R_{\max}$:

$$\mathbb{E}_{\pi_\theta}[R^* \mid \mathcal{U}] \geq \mathbb{E}_{\pi_\theta}[\hat{R} \mid \mathcal{U}] - \epsilon_{\text{risk}} - 4R_{\max} \cdot D_{\text{TV}}(\pi_\theta \parallel \pi_{\text{ref}} \mid \mathcal{U}) \quad (15)$$

Step 4: KL–TV connection. By Girsanov’s theorem, the KL divergence restricted to \mathcal{U} equals $\frac{1}{2}\mathcal{L}_{\text{KL}}$. Pinsker’s inequality then gives:

$$D_{\text{TV}} \leq \sqrt{\frac{1}{2}D_{\text{KL}}} = \frac{1}{2}\sqrt{\mathcal{L}_{\text{KL}}} \quad (16)$$

Step 5: Assembly. Combining Steps 1–4 with $\pi_\theta(\mathcal{U}^C) \leq 1$ yields the stated bound.

Theoretical Insight. Unlike global KL penalties that indiscriminately constrain all exploration, Astrolabe’s selective penalty acts only through the $\pi_\theta(\mathcal{U}) \cdot 2R_{\max}\sqrt{\mathcal{L}_{\text{KL}}}$ term. In safe regions ($x \notin \mathcal{U}$), the policy explores freely; the trust region activates only when π_θ drifts into the high-uncertainty region \mathcal{U} , naturally balancing exploration and stability.

C Algorithm

We provide the detailed pseudocode for the training procedures of the Astrolabe framework. Algorithm 1 outlines the core forward-process reinforcement learning pipeline, termed NFT Training with Selective KL Regularization. It details the multi-reward evaluation, uncertainty quantification via rank disagreement, and the selective application of the KL penalty to mitigate reward hacking

during short-clip optimization. To scale this alignment to long-sequence generation without exceeding memory constraints, Algorithm 2 presents the Streaming Training for Long Video. This algorithm leverages a rolling KV cache and detaches historical context, applying gradient updates exclusively to local active windows while maintaining long-range temporal coherence.

D More Qualitative Results

We present additional qualitative comparisons on 30-second long video generation under the single-prompt setting in Figures S2–S29. Qualitative comparisons showing improvements over baseline distilled models and competing methods. As shown in Figure S1, our method consistently produces higher-quality and more temporally coherent videos compared to the Krea 14B baseline [32], demonstrating that our approach yields notable improvements even when applied on top of large-scale 14B models.



Fig. S1: Qualitative comparison between Krea 14B (odd rows) and with our method (+Ours, even rows)

E Discussion

While Astrolabe establishes a robust and memory-efficient paradigm for aligning distilled autoregressive video models, several limitations warrant further investigation.

Reliance on the Capability of Reward Models. Astrolabe fundamentally depends on the accuracy of the selected reward models. Currently, open-source video evaluation models (e.g., VideoAlign) exhibit strong proficiency in assessing short-term aesthetics and text-video alignment. However, their ability to evaluate complex physics, long-horizon causality, and multi-entity interactions in minute-scale videos remains limited. Consequently, if the reward model fails to penalize subtle temporal hallucinations in extended sequences, Astrolabe cannot explicitly correct them. Developing more robust, physics-aware reward models for long-form video represents a critical next step for the community.

Inherent Bottlenecks of the Base Architecture. As a post-training RL framework, Astrolabe excels at shifting the generation distribution toward high-reward regions and mitigating error accumulation. However, reinforcement learning cannot arbitrarily instantiate capabilities that are entirely absent from the distilled base model. For instance, if the original streaming models (e.g., Self-Forcing or LongLive) inherently lack the capacity to render highly complex spatial geometries or specific domain knowledge due to extreme distillation, our method can optimize the presentation of existing knowledge but cannot overcome the fundamental capacity ceiling of the base architecture.

Algorithm 1 NFT Training with Selective KL Regularization

Require: Policy π_θ , behavior policy $\pi_{\theta_{\text{old}}}$, KL reference $\pi_{\theta_{\text{ref}}}$; reward functions $\{R_m\}_{m=1}^M$; prompts \mathcal{D} ; hyperparameters $\beta, \lambda_{\text{KL}}, K_{\text{max}}, \tau_{\text{KL}}$

Ensure: Optimized policy π_θ

- 1: Initialize $\theta_{\text{old}} \leftarrow \theta, \theta_{\text{ref}} \leftarrow \theta$
- 2: Initialize risk buffer $\mathcal{B} \leftarrow \emptyset$, KL ratio $\rho \leftarrow \rho_0, k_{\text{last}} \leftarrow 0$
- 3: **for** each epoch k **do**
- 4: // **Phase 1: Rollout and multi-reward evaluation**
- 5: Sample prompts $\{c_i\}_{i=1}^B \sim \mathcal{D}$
- 6: Generate samples $\{x_0^{(i)}\}$ using $\pi_{\theta_{\text{old}}}$
- 7: Compute rewards $\{r_m^{(i)} = R_m(x_0^{(i)}, c_i)\}$ for each reward model m
- 8: Compute advantages $\{A^{(i)}\}$ from primary reward
- 9: // **Compute reward uncertainty via rank disagreement**
- 10: **for** each reward model m **do**
- 11: $\text{rank}_m^{(i)} \leftarrow \text{Rank}(\{r_m^{(j)}\}_{j=1}^B)$ ▷ Rank samples by reward m
- 12: **end for**
- 13: $\Delta_{\text{rank}}^{(i)} \leftarrow \text{rank}_{\text{primary}}^{(i)} - \frac{1}{M-1} \sum_{m \neq \text{primary}} \text{rank}_m^{(i)}$
- 14: // **Adaptive threshold via risk compensation**
- 15: $\rho \leftarrow \text{UPDATERISKRATIO}(\mathcal{B}, \{\Delta_{\text{rank}}^{(i)}\}, \rho)$
- 16: $\tau \leftarrow \text{Percentile}(\{\Delta_{\text{rank}}^{(i)} | \Delta_{\text{rank}}^{(i)} \geq 0\}, 100 - 100\rho)$
- 17: $\mathcal{M}^{(i)} \leftarrow \mathbb{1}[\Delta_{\text{rank}}^{(i)} > \tau]$ ▷ High-uncertainty mask
- 18: // **Phase 2: Forward process optimization**
- 19: **for** each mini-batch (x_0, A, \mathcal{M}) **do**
- 20: Sample $t \sim \mathcal{U}(\mathcal{T})$
- 21: $x_t \leftarrow (1-t)x_0 + t\epsilon, \quad \epsilon \sim \mathcal{N}(0, I)$
- 22: $v_\theta, v_{\theta_{\text{old}}}, v_{\theta_{\text{ref}}} \leftarrow \pi_\theta(x_t, t), \pi_{\theta_{\text{old}}}(x_t, t), \pi_{\theta_{\text{ref}}}(x_t, t)$
- 23: // **Policy loss**
- 24: $v^+ \leftarrow \beta \cdot v_\theta + (1-\beta) \cdot v_{\theta_{\text{old}}}$
- 25: $v^- \leftarrow (1+\beta) \cdot v_{\theta_{\text{old}}} - \beta \cdot v_\theta$
- 26: $\tilde{r} \leftarrow \text{clip}(A/A_{\text{max}})/2 + 0.5$
- 27: $\mathcal{L}_{\text{policy}} \leftarrow \tilde{r} \|v^+ - x_0\|^2 + (1-\tilde{r}) \|v^- - x_0\|^2$
- 28: // **Selective KL: only on high-uncertainty samples**
- 29: $\mathcal{L}_{\text{KL}} \leftarrow \frac{1}{|\mathcal{M}|} \sum_{i: \mathcal{M}^{(i)}=1} \|v_\theta^{(i)} - v_{\theta_{\text{ref}}}^{(i)}\|^2$
- 30: $\mathcal{L} \leftarrow \mathcal{L}_{\text{policy}} + \lambda_{\text{KL}} \cdot \mathcal{L}_{\text{KL}}$
- 31: Update: $\theta \leftarrow \theta - \eta \nabla_\theta \mathcal{L}$
- 32: **end for**
- 33: // **Adaptive reference update based on KL divergence**
- 34: **if** $\mathcal{L}_{\text{KL}} > \tau_{\text{KL}}$ **or** $k - k_{\text{last}} > K_{\text{max}}$ **then**
- 35: $\theta_{\text{ref}} \leftarrow \theta$ ▷ Reset KL reference
- 36: $k_{\text{last}} \leftarrow k$
- 37: **end if**
- 38: $\theta_{\text{old}} \leftarrow \gamma \cdot \theta_{\text{old}} + (1-\gamma) \cdot \theta$
- 39: **end for**

Algorithm 2 Streaming Training for Long Video

Require: Policy π_θ , behavior policy $\pi_{\theta_{\text{old}}}$, KL reference $\pi_{\theta_{\text{ref}}}$; rewards $\{R_m\}$; prompts \mathcal{D} ; window size W , total frames F

Ensure: Optimized policy π_θ

- 1: Initialize $\theta_{\text{old}} \leftarrow \theta$, $\theta_{\text{ref}} \leftarrow \theta$, risk buffer $\mathcal{B} \leftarrow \emptyset$, $\rho \leftarrow \rho_0$
- 2: **for** each epoch k **do**
- 3: // **Select training window (synced across GPUs)**
- 4: $s \leftarrow \text{SELECTWINDOW}(F, W)$, $F_{\text{req}} \leftarrow s + W$
- 5: // **Phase 1: Efficient rollout with multi-reward**
- 6: Sample prompts $\{c_i\}_{i=1}^B \sim \mathcal{D}$
- 7: Generate partial videos $\{x_0^{(i)}[0 : F_{\text{req}}]\}$ using $\pi_{\theta_{\text{old}}}$
- 8: Extract window: $x_{0,W}^{(i)} \leftarrow x_0^{(i)}[s : s + W]$
- 9: Compute rewards $\{r_m^{(i)} = R_m(x_{0,W}^{(i)}, c_i)\}$ for each model m
- 10: Compute advantages $\{A^{(i)}\}$
- 11: // **Reward uncertainty via rank disagreement**
- 12: **for** each reward model m **do**
- 13: $\text{rank}_m^{(i)} \leftarrow \text{Rank}(\{r_m^{(j)}\}_{j=1}^B)$
- 14: **end for**
- 15: $\Delta_{\text{rank}}^{(i)} \leftarrow \text{rank}_{\text{primary}}^{(i)} - \frac{1}{M-1} \sum_{m \neq \text{primary}} \text{rank}_m^{(i)}$
- 16: $\rho \leftarrow \text{UPDATERISKRATIO}(\mathcal{B}, \{\Delta_{\text{rank}}^{(i)}\}, \rho)$
- 17: $\tau \leftarrow \text{Percentile}(\{\Delta_{\text{rank}}^{(i)} \geq 0\}, 100 - 100\rho)$
- 18: $\mathcal{M}^{(i)} \leftarrow \mathbb{1}[\Delta_{\text{rank}}^{(i)} > \tau]$
- 19: // **Phase 2: Window-focused optimization with selective KL**
- 20: **for** each mini-batch (x_0, A, \mathcal{M}) **do**
- 21: Sample $t \sim \mathcal{U}(T)$, $x_t \leftarrow (1-t)x_0 + t\epsilon$
- 22: $v_\theta, v_{\theta_{\text{old}}}, v_{\theta_{\text{ref}}} \leftarrow \text{STREAMINGNFT}(x_t, t, s, W)$
- 23: Extract: $v_{\theta,W}, v_{\theta_{\text{old}},W}, v_{\theta_{\text{ref}},W}, x_{0,W}$
- 24: // **Policy loss on window**
- 25: $v^+ \leftarrow \beta \cdot v_{\theta,W} + (1-\beta) \cdot v_{\theta_{\text{old}},W}$
- 26: $v^- \leftarrow (1+\beta) \cdot v_{\theta_{\text{old}},W} - \beta \cdot v_{\theta,W}$
- 27: $\tilde{r} \leftarrow \text{clip}(A/A_{\text{max}})/2 + 0.5$
- 28: $\mathcal{L}_{\text{policy}} \leftarrow \tilde{r} \|v^+ - x_{0,W}\|^2 + (1-\tilde{r}) \|v^- - x_{0,W}\|^2$
- 29: // **Selective KL on high-uncertainty samples**
- 30: $\mathcal{L}_{\text{KL}} \leftarrow \frac{1}{|\mathcal{M}|} \sum_{i: \mathcal{M}^{(i)}=1} \|v_{\theta,W}^{(i)} - v_{\theta_{\text{ref}},W}^{(i)}\|^2$
- 31: Update: $\theta \leftarrow \theta - \eta \nabla_\theta (\mathcal{L}_{\text{policy}} + \lambda_{\text{KL}} \mathcal{L}_{\text{KL}})$
- 32: **end for**
- 33: // **Adaptive reference update**
- 34: **if** $\mathcal{L}_{\text{KL}} > \tau_{\text{KL}}$ **or** $k - k_{\text{last}} > K_{\text{max}}$ **then**
- 35: $\theta_{\text{ref}} \leftarrow \theta$, $k_{\text{last}} \leftarrow k$
- 36: **end if**
- 37: $\theta_{\text{old}} \leftarrow \gamma \cdot \theta_{\text{old}} + (1-\gamma) \cdot \theta$
- 38: **end for**

Photorealistic closeup video of two pirate ships battling each other as they sail inside a cup of coffee.



Extreme close up of a 24 year old woman's eye blinking, standing in Marrakech during magic hour, cinematic film shot in 70mm, depth of field, vivid colors, cinematic

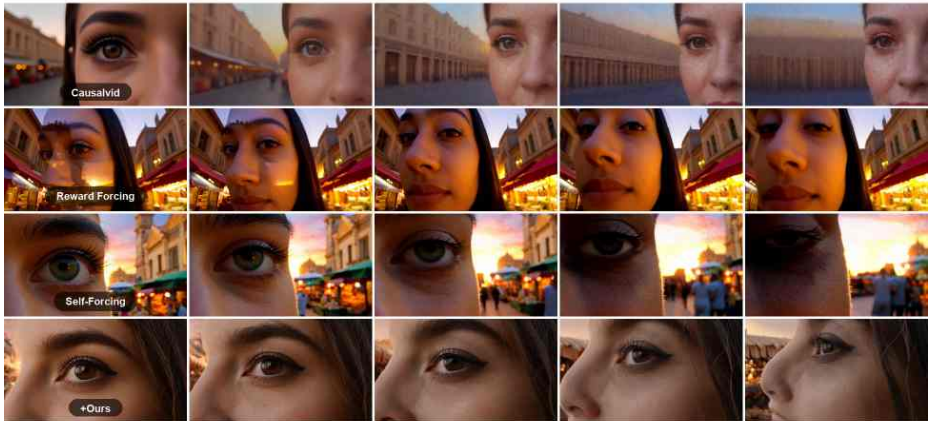
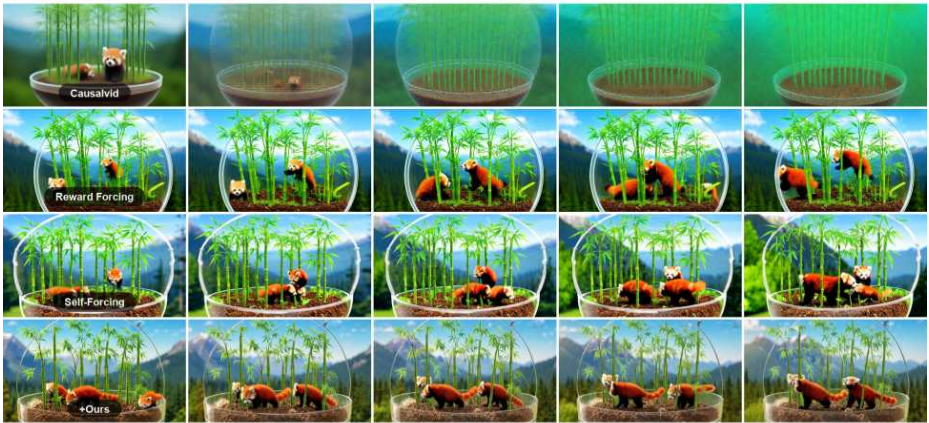


Fig. S2: Qualitative comparison on long video generation (30s) under the single-prompt setting (Set 1).

A petri dish with a bamboo forest growing within it that has tiny red pandas running around.



A Chinese Lunar New Year celebration video with Chinese Dragon.



Fig. S3: Additional qualitative comparison on long video generation (30s) under the single-prompt setting (Set 2).

The Glenfinnan Viaduct is a historic railway bridge in Scotland, UK, that crosses over the west highland line between the towns of Mallaig and Fort William. It is a stunning sight as a steam train leaves the bridge, traveling over the arch-covered viaduct. The landscape is dotted with lush greenery and rocky mountains, creating a picturesque backdrop for the train journey. The sky is blue and the sun is shining, making for a beautiful day to explore this majestic spot.

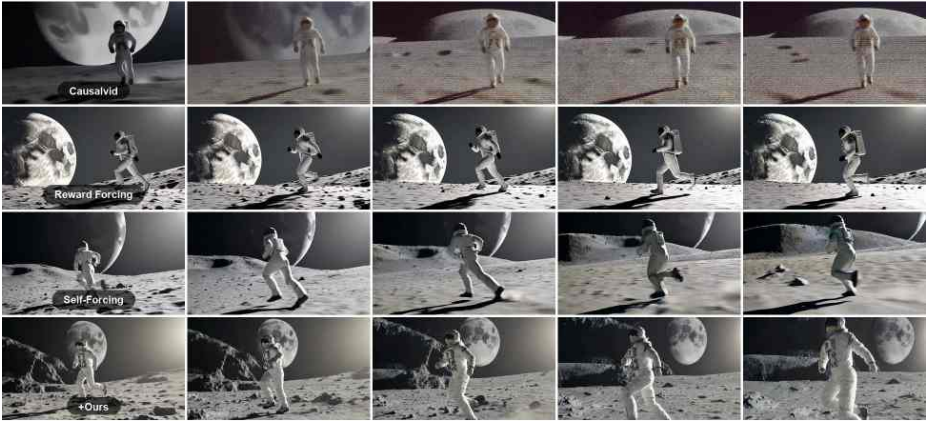


A white cat driving in a car through a busy downtown street with tall buildings and pedestrians in the background



Fig. S4: Additional qualitative comparison on long video generation (30s) under the single-prompt setting (Set 3).

An astronaut runs on the surface of the moon, the low angle shot shows the vast background of the moon, the movement is smooth and appears lightweight



Close up shot of a living flame wisp darting through a bustling fantasy market at night.



Fig. S5: Additional qualitative comparison on long video generation (30s) under the single-prompt setting (Set 4).

A first-person POV shot rapidly flies towards a house's front door at 10x speed.



A giant humanoid, made of fluffy blue cotton candy, stomping on the ground, and roaring to the sky, clear blue sky behind them.



Fig. S6: Additional qualitative comparison on long video generation (30s) under the single-prompt setting (Set 5).

A man standing in front of a burning building giving the 'thumbs up' sign.



humans walking into a dragon's open jaws descending into the underworld

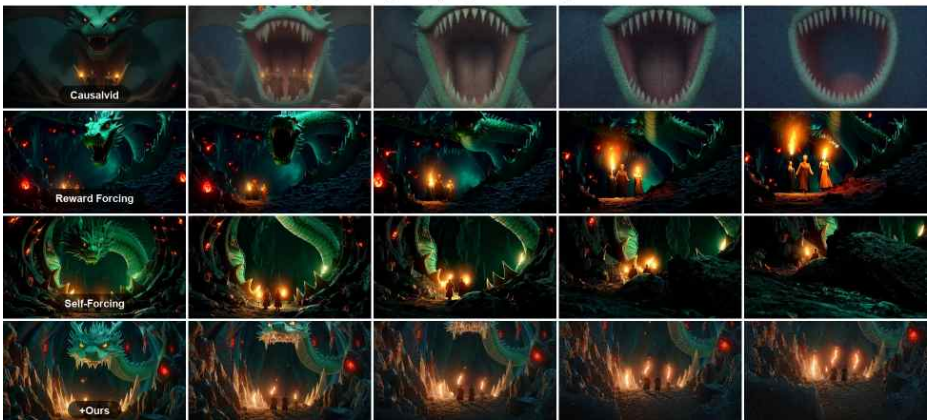


Fig. S7: Additional qualitative comparison on long video generation (30s) under the single-prompt setting (Set 6).

A chimp on the sidewalk doing a backflip on a skateboard.



A truck rolling backwards down a hill while a family chases it with balloons and cakes in their arms.



Fig. S8: Additional qualitative comparison on long video generation (30s) under the single-prompt setting (Set 7).

Top view timelapse video of an artwork being drawn by hand with colored markers, the artwork shows a dragon flying over a castle



A red panda taking a bite of a pizza



Fig. S9: Additional qualitative comparison on long video generation (30s) under the single-prompt setting (Set 8).

A cute golden dragon is walking like a model on stage, and the audience is clapping for him.



A female warrior rushes towards the camera, and suddenly she turns into a holographic monster.

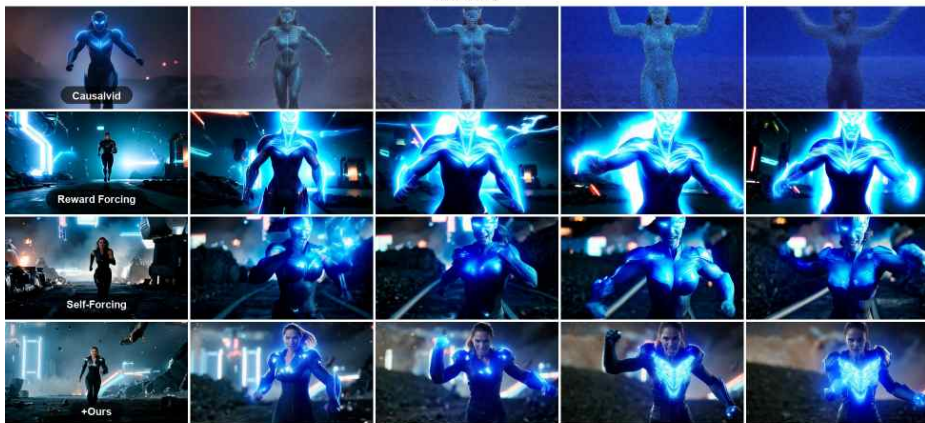


Fig. S10: Additional qualitative comparison on long video generation (30s) under the single-prompt setting (Set 9).

A man is eating salad



A car is on fire and exploding.



Fig. S11: Additional qualitative comparison on long video generation (30s) under the single-prompt setting (Set 10).

A red bird transforms into a flag



A curtain transforms into a dancing girl



Fig. S12: Additional qualitative comparison on long video generation (30s) under the single-prompt setting (Set 11).

a photorealistic video of a butterfly that can swim navigating underwater through a beautiful coral reef



a walking figure made out of water tours an art gallery with many beautiful works of art in different styles



Fig. S13: Additional qualitative comparison on long video generation (30s) under the single-prompt setting (Set 12).

An ethereal moment as a figure is tethered to a majestic butterfly, soaring through a cosmic night filled with floating petals and vibrant colors, symbolizing the delicate balance between dreams and reality



Close-up of a majestic white dragon with pearlescent, silver-edged scales, icy blue eyes, elegant ivory horns, and misty breath. Focus on detailed facial features and textured scales, set against a softly blurred background

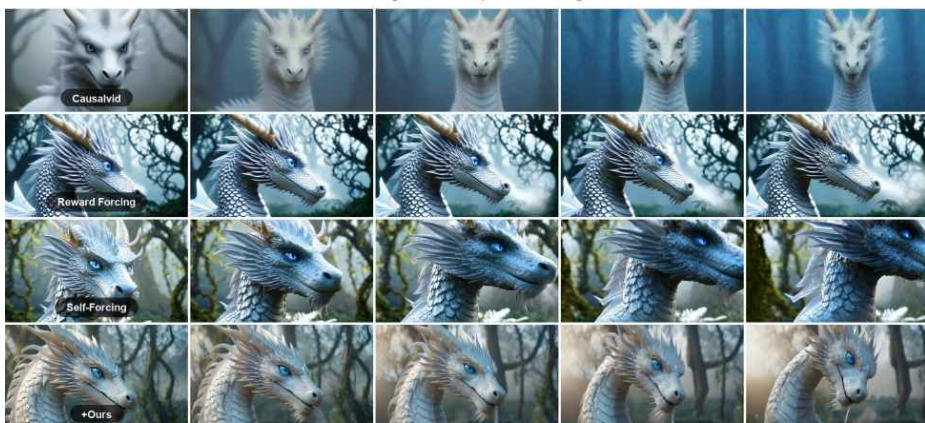


Fig. S14: Additional qualitative comparison on long video generation (30s) under the single-prompt setting (Set 13).

a tortoise whose body is made of glass, with cracks that have been repaired using kintsugi, is walking on a black sand beach at sunset



A dynamic motion shot of a paper airplane morphing into a swan. The pointed nose becomes a graceful neck and head, wings unfolding and expanding. The camera moves around as the flat surfaces gain volume, creases softening into feathers. The tail section splits into webbed feet. The transformation finishes as the swan's plumage turns pristine white, its beak forming from the paper's final fold.

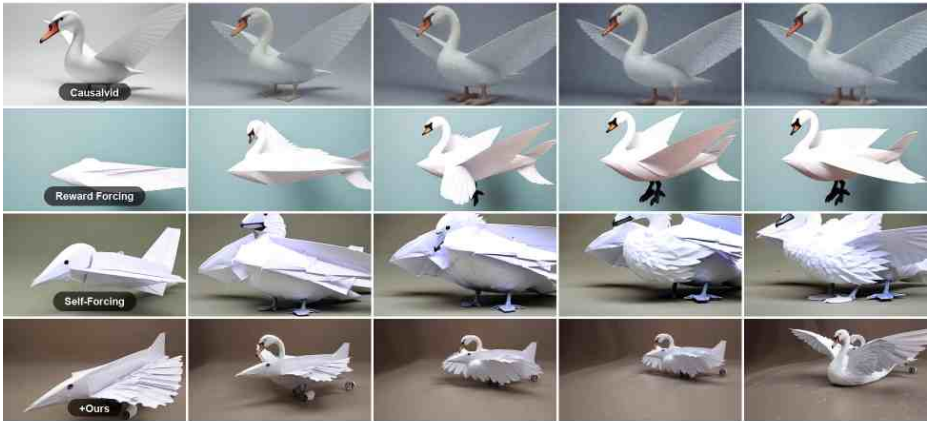


Fig. S15: Additional qualitative comparison on long video generation (30s) under the single-prompt setting (Set 14).

A hot air balloon descending back to the ground.



Flying cars zoom through a futuristic cityscape, maneuvering around towering skyscrapers while lights flicker on the buildings, creating a constantly shifting pattern.

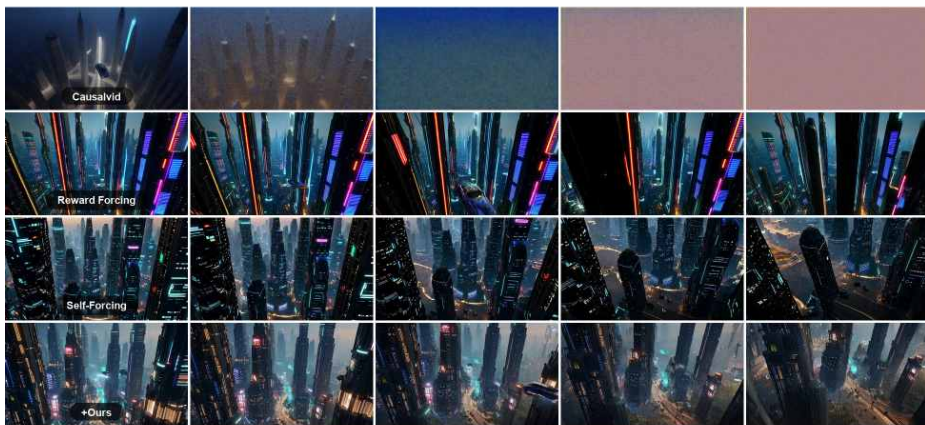


Fig. S16: Additional qualitative comparison on long video generation (30s) under the single-prompt setting (Set 15).

A medieval castle overlooking a bustling renaissance fair.



A post-apocalyptic city overrun by nature, with vines covering buildings.



Fig. S17: Additional qualitative comparison on long video generation (30s) under the single-prompt setting (Set 16).

A vibrant carnival buzzes with activity as people enjoy rides, play games, and admire colorful lights, the energy and excitement filling the air.



A futuristic city park features holographic art installations, with people walking through, pausing to admire the digital displays that blend seamlessly with the natural surroundings.



Fig. S18: Additional qualitative comparison on long video generation (30s) under the single-prompt setting (Set 17).

People stroll along a vibrant city street, neon signs flashing and flickering overhead as cars pass by, and pedestrians weave through the bustling nightlife.



A fish driving a tiny submarine, exploring an underwater city.



Fig. S19: Additional qualitative comparison on long video generation (30s) under the single-prompt setting (Set 18).

A monkey dressed as an astronaut, floating in a space station while juggling bananas.



A butterfly in a tiny race car, speeding around a track made of flowers.



Fig. S20: Additional qualitative comparison on long video generation (30s) under the single-prompt setting (Set 19).

A person painting a sunset in the sky with a giant paintbrush.



A person playing a grand piano underwater in a crystal-clear lake.



Fig. S21: Additional qualitative comparison on long video generation (30s) under the single-prompt setting (Set 20).

A person fishing for stars in a night sky with a glowing fishing rod.



A person playing an electric guitar made of lightning, with thunderous sound waves.



Fig. S22: Additional qualitative comparison on long video generation (30s) under the single-prompt setting (Set 21).

A person holding an umbrella that turns rain into colorful confetti.



A person riding a giant tortoise through a desert of glass sand.



Fig. S23: Additional qualitative comparison on long video generation (30s) under the single-prompt setting (Set 22).

A person playing a drum set made of thunderclouds, with each beat creating a lightning flash.



Two people on roller skates colliding in a rink, both spinning out of control.



Fig. S24: Additional qualitative comparison on long video generation (30s) under the single-prompt setting (Set 23).

A surfer accelerating on a wave, carving through the water.



An astronaut fighting a large dinosaur



Fig. S25: Additional qualitative comparison on long video generation (30s) under the single-prompt setting (Set 24).

Macro shot of a man wearing an antique diving helmet with dark glass and a jetpack walking on lava as a dragon flies behind him in the sky. Realistic style



An arc shot around a bonfire on a beach at night, with friends laughing and dancing in the flickering light.



Fig. S26: Additional qualitative comparison on long video generation (30s) under the single-prompt setting (Set 25).

A zoom-out from a single person standing in the middle of a desert, revealing the expansive, empty sand dunes around them.



A pull-out from a dancer's feet moving gracefully, expanding to show the entire stage and audience.



Fig. S27: Additional qualitative comparison on long video generation (30s) under the single-prompt setting (Set 26).

a toy robot wearing blue jeans and a white t shirt taking a pleasant stroll in Antarctica during a colorful festival



a woman wearing a green dress and a sun hat taking a pleasant stroll in Johannesburg South Africa during a winter storm



Fig. S28: Additional qualitative comparison on long video generation (30s) under the single-prompt setting (Set 27).

an adorable kangaroo wearing purple overalls and cowboy boots taking a pleasant stroll in Mumbai India during a colorful festival



an adorable kangaroo wearing a green dress and a sun hat taking a pleasant stroll in Johannesburg South Africa during a colorful festival



Fig. S29: Additional qualitative comparison on long video generation (30s) under the single-prompt setting (Set 28).